Acta Materialia 245 (2023) 118658

Contents lists available at ScienceDirect

Acta Materialia

journal homepage: www.elsevier.com/locate/actamat

Full length article

A finite element method to calculate geometrically necessary dislocation density: Accounting for orientation discontinuities in polycrystals

Eralp Demir [a,b,*], Edward William Horton [b], Anna Kareer [c], David M. Collins [d], Mahmoud Mostafavi [b], David Knowles [b]

[a] Department of Engineering Science, University of Oxford, Parks road, Oxford OX1 3PJ, UK
[b] Department of Mechanical Engineering, University of Bristol, Bristol, BS8 1TR, UK
[c] Department of Materials, University of Oxford, Parks Road, Oxford OX1 3PH, UK
[d] School of Metallurgy and Materials, University of Birmingham, Edgbaston, Birmingham B15 2TT, UK

ARTICLE INFO

Keywords:
Finite element method
Geometrically-necessary dislocations
Orientation gradients
Polycrystals

ABSTRACT

Strain gradients have been used to link various microscale deformation phenomena to the mechanical response of a polycrystalline material, revealing sub-crystal deformation structures. The strain gradients are computed in terms of the orientation gradients and then converted to geometrically necessary dislocation densities, a quantity considered important to explain flow stress and strain hardening behaviour. In this study, a unique method has been developed to compute the orientation gradients by finite element method while enforcing orientation continuity inside the grains and allowing sharp gradients at the grain boundaries by a global minimization approach. The method is showcased on an exemplar electron backscatter diffraction datasets of a stainless type of steel. The energy minimization method (Demir et al., 2009) reveals geometrically necessary dislocation densities that are an order of magnitude lower than those calculated using the widely accepted Least-Squares minimization approach (Arsenlis et al., 1999). The proposed approach successfully eliminates sharp orientation gradients at grain boundaries, removing the artificially high dislocation densities near orientation discontinuities that is characteristic to the finite difference-based approaches.

1. Introduction

Strain gradients have been used to correlate the mechanical behaviour of a wide-range of single crystal and polycrystals materials, for both single and multi-phases [1]. A few example applications include the size dependence of flow stress in single crystals [2], the mechanical behaviour of multi-phase materials [3,4], and grain size dependence for polycrystals [5].

The strain gradients are correlated to mechanical strength using Taylor's equation ($\tau_c = \alpha G b\sqrt{\varrho}$). According to Taylor, an increase in the dislocation density or decrease in the mean spacing between dislocations, leads to a decrease the critical bow out radius as the physical source of the corresponding increase in the critical strength ϱ[6]. The strain gradients can be expressed in terms of the density of geometrically necessary dislocations (GNDs); these are defined, as the name suggests, as the dislocations that are geometrically needed to accommodate the lattice curvature [7]. As a first order effect, the GNDs increase both the flow stress and strain hardening as dislocations become more closely spaced [8]. Backstress is a second order effect arising from the inhomogeneous distribution of GNDs, causing polarized dislocation structures [9]. Given the perceived role of strain gradients in explaining microscale behaviour that governs the macroscopic response, obtaining accurate measurements of GND densities at appropriate length scales is highly desirable.

GNDs can be computed from either the elastic or the plastic incompatibility. Most of the current computational studies use the plastic incompatibility as the measure for GNDs since the slip rates are numerically available [10–12]. The curl of the vector field mapped by the plastic deformation gradient ($\nabla \times \mathbf{F_p}$) remains a widely-accepted method for the calculation of the lattice curvature [13] and strain gradients, based on the original studies of Dai and Parks [14]. In some computational studies, slip gradients were used as a more direct measure for lattice incompatibility [15,16]. The elastic part of the deformation gradient has also been used as the measure for strain gradients [17]. The dislocation flux, that is defined as the convective part of the lattice incompatibility [18], was also used to compute as a measure for GND density in a deforming polycrystal [19,20]. A further detailed overview of the calculation procedures for incompatibility

* Corresponding author at: Department of Engineering Science, University of Oxford, Parks road, Oxford OX1 3PJ, UK.
E-mail address: eralp.demir@eng.ox.ac.uk (E. Demir).

https://doi.org/10.1016/j.actamat.2022.118658
Received 31 August 2022; Received in revised form 26 November 2022; Accepted 24 December 2022
Available online 27 December 2022

and GND density in numerical crystal plasticity simulations can be found [21].

Common experimental measurements of local strain can be distinguished into two categories: **i.** real space methods such as Digital Image Correlation (DIC) where the total strain is obtained from surface displacements [22–24] and **ii.** reciprocal space measurements such as electron-backscatter diffraction (EBSD) to obtain the local crystal orientation and distortion (elastic strain) [25,26]. For such experiments, the elastic part of the deformation consisting of both lattice rotation and elastic strain components are used to compute the lattice incompatibility [27]. Utilizing this property, intragranular crystal orientations [28,29] and residual elastic strains with spatial resolution better than 100 nm [25,30] have been performed with EBSD. The orientation gradients have been widely used as the sole measure for incompatibility [31]. In this particular approach, the elastic distortions were neglected allowing determination of incompatibility from the lattice rotations, which is reasonable for metals having small elastic strains. Thus, the GND density can be obtained from the local crystal orientation measurements and their gradients. Equivalent detail can also be obtained in three-dimensions using other crystal orientation measurement techniques such as X-ray Diffraction Contrast Tomography (DCT) [32], Differential Aperture X-ray Laue Micro-diffraction (DAXM) [33] and Dark Field X-ray Microscopy (DFXM) [34]. Although experimental techniques have evolved significantly over the last decade, the method to compute the orientation gradients have not changed significantly. The orientation gradients have been computed using finite difference approaches in almost all of the recent studies [35–43].

In this method, the gradients are computed using the difference between data points. Calculation of gradients with a higher degree of accuracy was achieved by utilizing different neighbourhood relationships including data points that are not simply the nearest neighbours [44,45]. More recently, a finite element method has been used to compute the orientation gradients [46], where the divergence of the crystal orientation field was used as the measure for incompatibility, similar to the studies of Field et al. [29].

Errors or large fluctuations in any orientation measurements can lead to incorrect conclusions, hence, these must be minimized by adopting a consistent framework. For a polycrystalline material, the orientations are generally (1) continuous within grains, even when plasticity is high, and (2) possess a sharp orientation discontinuity at a grain boundary. As an artefact of the latter, a sharp local misorientation gives rise to artificially steep gradients that falsely predict high GND densities. Whilst they are not physically present, their inclusion is a consequence of the mathematics of a finite difference approach. A new approach is developed in this study which aims to addresses the shortcomings of the finite difference approach and is referred to as Orientation GRadiEnts by Finite Element Method (OGRE-FEM). Here, a finite element method is adopted with the crystal orientation being the field variable. The proposed method employs a global minimization between the field quantity and the measured orientations; it further enforces orientation continuity within grains, and accounts for sharp orientation changes at grain boundaries. This calculation procedure has significant relevance to practical applications such as the prediction of failure of structurally critical engineering materials.

2. Method (OGRE-FEM)

2.1. Crystal orientation and its gradient

Local crystal orientations can be expressed with angle-axis form with an angle, θ, and a rotation axis $\{\mathbf{r}\}$, in Eq. (1):

$$\{\mathbf{r}\} = \begin{Bmatrix} u & v & w \end{Bmatrix}^T. \tag{1}$$

where u, v and w are the indices of a direction vector in the crystal. The field variable in this analysis is the angle-axis pair which is indicated with $\{\mathbf{d}\}$ in four degrees of freedom in Eq. (2):

$$\{\mathbf{d}\} = \begin{Bmatrix} u & v & w & \theta \end{Bmatrix}^T. \tag{2}$$

The axis vector shall satisfy the inequality constrains in Eq. (3) to remain within the unit stereographic triangle:

$$0 \le w \le v \le u \le 1. \tag{3}$$

The orientation matrix in the crystal frame, $[\mathbf{g}]$, is computed using the angle and axis pair in Eq. (4):

$$[\mathbf{g}] = \begin{bmatrix} \cos\theta + u^2(1-\cos\theta) & uv(1-\cos\theta) + w\sin\theta & uw(1-\cos\theta) - v\sin\theta \\ uv(1-\cos\theta) - w\sin\theta & \cos\theta + v^2(1-\cos\theta) & vw(1-\cos\theta) + u\sin\theta \\ uw(1-\cos\theta) + v\sin\theta & vw(1-\cos\theta) - u\sin\theta & \cos\theta + w^2(1-\cos\theta) \end{bmatrix}. \tag{4}$$

The variation of the vectorized crystal orientation components, $\{\mathbf{g}\}$, with respect to field variables, angle-axis pair, is obtained by differentiation,[1] as given in Eq. (5):

$$\begin{aligned}
\delta g_{11} &= (u^2-1)\sin\theta\delta\theta + 2(1-\cos\theta)u\delta u, \\
\delta g_{12} &= (uv\sin\theta + w\cos\theta)\delta\theta + (1-\cos\theta)v\delta u + (1-\cos\theta)u\delta v + \sin\theta\delta w, \\
\delta g_{13} &= (uw\sin\theta - v\cos\theta)\delta\theta + (1-\cos\theta)w\delta u - \sin\theta\delta v + u(1-\cos\theta)\delta w, \\
\delta g_{21} &= (vu\sin\theta - w\cos\theta)\delta\theta + (1-\cos\theta)v\delta u + (1-\cos\theta)u\delta v - \sin\theta\delta w, \\
\delta g_{22} &= (v^2-1)\sin\theta\delta\theta + 2(1-\cos\theta)v\delta v, \\
\delta g_{23} &= (vw\sin\theta + u\cos\theta)\delta\theta + \sin\theta\delta u + w(1-\cos\theta)\delta v + v(1-\cos\theta)\delta w, \\
\delta g_{31} &= (wu\sin\theta + v\cos\theta)\delta\theta + (1-\cos\theta)w\delta u + \sin\theta\delta v + u(1-\cos\theta)\delta w, \\
\delta g_{32} &= (vw\sin\theta - u\cos\theta)\delta\theta - \sin\theta\delta u + w(1-\cos\theta)\delta v + v(1-\cos\theta)\delta w, \\
\delta g_{33} &= (w^2-1)\sin\theta\delta\theta + 2(1-\cos\theta)w\delta w.
\end{aligned} \tag{5}$$

Eq. (5) can be simplified and expressed via gradient mapping, $[\mathbf{G}]$, given in Eq. (6):

$$\begin{Bmatrix} \delta g_{11} \\ \delta g_{12} \\ \delta g_{13} \\ \delta g_{21} \\ \delta g_{22} \\ \delta g_{23} \\ \delta g_{31} \\ \delta g_{32} \\ \delta g_{33} \end{Bmatrix} = [\mathbf{G}] \begin{Bmatrix} \delta u \\ \delta v \\ \delta w \\ \delta\theta \end{Bmatrix}. \tag{6}$$

where $[\mathbf{G}]$ is the gradient mapping in terms of the angle-axis pair, Eq. (7):

$$[\mathbf{G}] = \begin{bmatrix} 2(1-\cos\theta)u & 0 & 0 & (u^2-1)\sin\theta \\ (1-\cos\theta)v & (1-\cos\theta)u & \sin\theta & uv\sin\theta + w\cos\theta \\ (1-\cos\theta)w & -\sin\theta & u(1-\cos\theta) & uw\sin\theta - v\cos\theta \\ (1-\cos\theta)v & (1-\cos\theta)u & -\sin\theta & vu\sin\theta - w\cos\theta \\ 0 & 2(1-\cos\theta)v & 0 & (v^2-1)\sin\theta \\ \sin\theta & w(1-\cos\theta) & v(1-\cos\theta) & vw\sin\theta + u\cos\theta \\ (1-\cos\theta)w & \sin\theta & u(1-\cos\theta) & wu\sin\theta + v\cos\theta \\ -\sin\theta & w(1-\cos\theta) & v(1-\cos\theta) & vw\sin\theta - u\cos\theta \\ 0 & 0 & 2(1-\cos\theta)w & (w^2-1)\sin\theta \end{bmatrix}. \tag{7}$$

2.2. Local form of orientation field

The objective in this study is to minimize the difference between the measured and computed orientation fields, as described by the spatially local orientation residual in Eq. (8). The brackets are not used in this section for clarity. $\tilde{\mathbf{d}}$ denotes the experimentally measured, or known

[1] The partial differential operator δ represents the variation while ∇ represents the gradient operator.

values of orientations, and $\mathbf{d}(\mathbf{x})$ represents the field variable vector to be identified:

$$\mathbf{d}(\mathbf{x}) - \widetilde{\mathbf{d}} = \mathbf{0}. \tag{8}$$

An additional constraint on the gradient of orientations is used to ensure the continuity of the lattice by using the local form in Eq. (9). This helps to reduce the experimental errors or uncertainties. The orientation gradients are computed using the field variable, $\mathbf{d}(\mathbf{x})$, and the gradient mapping for all three directions, $\boldsymbol{\Gamma}$, to give Eq. (9).

$$\boldsymbol{\nabla}\mathbf{g}(\mathbf{x}) = \boldsymbol{\Gamma}(\mathbf{x})\,\boldsymbol{\nabla}\mathbf{d}(\mathbf{x}) = \mathbf{0}. \tag{9}$$

$\boldsymbol{\Gamma}(\mathbf{x})$ is coefficient for the independent gradients that is constructed using the gradient mapping, $[\mathbf{G}]$, as in Eq. (10). Note that the $\boldsymbol{\Gamma}(\mathbf{x})$ applies to the orientation gradients in three principal directions:

$$\boldsymbol{\Gamma}(\mathbf{x}) = \begin{bmatrix} [\mathbf{G}] & \mathbf{0} & \mathbf{0} \\ \mathbf{0} & [\mathbf{G}] & \mathbf{0} \\ \mathbf{0} & \mathbf{0} & [\mathbf{G}] \end{bmatrix}. \tag{10}$$

Finally, both constraints in Eqs. (8) and (9) are added and rearranged to obtain the local form of the overall expression that is solved, as given in Eq. (11):

$$[\mathbf{I} + \lambda\,\boldsymbol{\Gamma}(\mathbf{x})\,\boldsymbol{\nabla}\,]\,\mathbf{d}(\mathbf{x}) = \widetilde{\mathbf{d}}. \tag{11}$$

where λ represents the penalty factor for the orientation continuity constraint and $\mathbf{I}$ is the 2nd rank identity tensor.

2.3. Discrete form of orientation field

Eq. (12) shows the discretization of the angle-axis pair with independent degrees of freedom from each other using finite elements that are prescribed by the interpolation functions, $\{\mathbf{N}(\mathbf{x})\}^T$. The interpolation functions are shown in Appendix A. The symbols $\widetilde{u}$, $\widetilde{v}$, and $\widetilde{w}$ represent values of the axis vector components along the nodes, in the x, y, and z directions, respectively:

$$\begin{aligned} u(\mathbf{x}) &= \{\mathbf{N}(\mathbf{x})\}\,\{\widetilde{\mathbf{u}}\}, \\ v(\mathbf{x}) &= \{\mathbf{N}(\mathbf{x})\}\,\{\widetilde{\mathbf{v}}\}, \\ w(\mathbf{x}) &= \{\mathbf{N}(\mathbf{x})\}\,\{\widetilde{\mathbf{w}}\}, \\ \theta(\mathbf{x}) &= \{\mathbf{N}(\mathbf{x})\}\,\{\widetilde{\theta}\}. \end{aligned} \tag{12}$$

Similarly, the orientation gradients are calculated in terms of the discrete angle-axis components using the derivatives of the interpolation functions, $\nabla\mathbf{N}(\mathbf{x})$, shown in Eq. (13):

$$\begin{aligned} \{\boldsymbol{\nabla}\mathbf{u}(\mathbf{x})\} &= [\nabla\mathbf{N}(\mathbf{x})]\,\{\widetilde{\mathbf{u}}\}, \\ \{\boldsymbol{\nabla}\mathbf{v}(\mathbf{x})\} &= [\nabla\mathbf{N}(\mathbf{x})]\,\{\widetilde{\mathbf{v}}\}, \\ \{\boldsymbol{\nabla}\mathbf{w}(\mathbf{x})\} &= [\nabla\mathbf{N}(\mathbf{x})]\,\{\widetilde{\mathbf{w}}\}, \\ \{\boldsymbol{\nabla}\boldsymbol{\theta}(\mathbf{x})\} &= [\nabla\mathbf{N}(\mathbf{x})]\,\{\widetilde{\boldsymbol{\theta}}\}. \end{aligned} \tag{13}$$

The angle-axis pair is a unit vector which reveals a constraint on its components, u, v, and w. However, this does not limit the interpolation between individual components of the axis vector among unit vector fields. This 'unit vector' requirement is ensured by normalizing the angle-axis pairs after the interpolation.

Eq. (14) is used to calculate the gradient of the field variables. Only gradient computation along the x-direction is shown to avoid complexity. The subscript m indicates the number of nodes per finite element. The $\nabla_x\mathbf{N}_1$ represents the mapping for the calculation of the gradient along the x direction, corresponding to the 1st node:

$$\begin{Bmatrix} \nabla_x u(\mathbf{x}) \\ \nabla_x v(\mathbf{x}) \\ \nabla_x w(\mathbf{x}) \\ \nabla_x \theta(\mathbf{x}) \end{Bmatrix} = \begin{bmatrix} \nabla_x N_1 & 0 & 0 & 0 & \cdots & \nabla_x N_m & 0 & 0 & 0 \\ 0 & \nabla_x N_1 & 0 & 0 & \cdots & 0 & \nabla_x N_m & 0 & 0 \\ 0 & 0 & \nabla_x N_1 & 0 & \cdots & 0 & 0 & \nabla_x N_m & 0 \\ 0 & 0 & 0 & \nabla_x N_1 & \cdots & 0 & 0 & 0 & \nabla_x N_m \end{bmatrix} \times \begin{Bmatrix} \widetilde{u}_1 \\ \widetilde{v}_1 \\ \widetilde{w}_1 \\ \widetilde{\theta}_1 \\ \vdots \\ \widetilde{u}_m \\ \widetilde{v}_m \\ \widetilde{w}_m \\ \widetilde{\theta}_m \end{Bmatrix}. \tag{14}$$

Multiplication of the local form in Eq. (11) with the weight functions followed by the integration over the domain reveals the global constraint relation in Eq. (15). This contains three terms; **i.** a least-squares term, $\mathbf{M}$, also referred as the mass matrix, **ii.** a gradient term, $\mathbf{C}$, for the field variable, $\{\mathbf{d}\}$ through a Lagrangian constraint with a penalty factor, and λ, **iii.** a weighted vector of given quantities, $\mathbf{q}$, on the right hand-side of Eq. (15):

$$([\mathbf{M}] + \lambda\,[\mathbf{C}])\,\{\mathbf{d}\} = \{\mathbf{q}\}. \tag{15}$$

The mass matrix is computed using the interpolation functions, as in Eq. (16), which is also referred to as 'least-squares FEM' in the literature [47]. A simple derivation of the approach is shown in Appendix B.

$$[\mathbf{M}] = \int_{\Omega} [\mathbf{N}]^T\,[\mathbf{N}]\,\mathrm{d}\Omega. \tag{16}$$

The gradient mapping helps to obtain a smooth orientation field by weakly penalizing the gradients over the domain using Eq. (17):

$$[\mathbf{C}] = \int_{\Omega} [\nabla\mathbf{N}]^T\,[\boldsymbol{\Gamma}]^T\,[\boldsymbol{\Gamma}]\,[\boldsymbol{\nabla}\mathbf{N}]\,\mathrm{d}\Omega. \tag{17}$$

The measured orientations in the form of the field variables, $\widetilde{\mathbf{d}}$, are used to construct a pseudo-force vector, as in Eq. (18):

$$\{\mathbf{q}\} = \int_{\Omega} [\mathbf{N}]\,\{\widetilde{\mathbf{d}}\}\,\mathrm{d}\Omega. \tag{18}$$

After solving Eq. (15) for the field variable $\{\mathbf{d}\}$, the orientation gradients can be obtained using the field variable, Eq. (19):

$$\left[\boldsymbol{\nabla}\mathbf{g}\right] = [\boldsymbol{\Gamma}]\,[\boldsymbol{\nabla}\mathbf{N}]\,\{\mathbf{d}\}. \tag{19}$$

The least-squares finite element approach was applied in different prior studies; details of the method are given elsewhere [48–50].

Linear quadrilateral type elements were used in the analysis. Higher order quadrilateral type elements could also be used but not preferred since they increase the computational time. Similarly, triangular elements can be adopted for grids in hexagonal shape of EBSD measurements. The number of elements were the same as in the EBSD data points. The coarsening of the mesh size can be done outside this analysis using the any available EBSD data analysis software.

2.4. GND density calculation

The GND tensor is defined as the sum of the dislocation lines over a volume, V as in Eq. (20) [7,51]. $\mathbf{b}^i$ represents the slip direction having a magnitude of the Burgers vector. $\hat{\mathbf{t}}^i$ is the unit dislocation line direction for the ith system, Table Table 1:

$$\boldsymbol{\alpha} = \frac{1}{V}\sum_{i=1}^{18} \mathbf{b}^i \otimes \int_L \hat{\mathbf{t}}^i\,\mathrm{d}L. \tag{20}$$

The total dislocation line length divided by the volume of the domain defines the density of GNDs, ϱ^i_{GND}, of each dislocation system

Table 1
Dislocation configurations defined by slip direction, $\mathbf{b}^i$, and line direction, $\hat{\mathbf{t}}^i$, for FCC materials.

Type	Edge												Screw					
No.	1	2	3	4	5	6	7	8	9	10	11	12	13	14	15	16	17	18
$\hat{\mathbf{t}}^i$	$\bar{1}\bar{1}2$	$\bar{1}2\bar{1}$	$2\bar{1}\bar{1}$	$\bar{1}1\bar{2}$	$\bar{1}\bar{2}1$	211	$1\bar{1}\bar{2}$	121	$\bar{2}\bar{1}1$	112	$1\bar{2}\bar{1}$	$\bar{2}1\bar{1}$	110	101	011	$\bar{1}10$	$10\bar{1}$	$0\bar{1}1$
$\mathbf{b}^i$	$\bar{1}10$	$10\bar{1}$	$0\bar{1}1$	$\bar{1}\bar{1}0$	101	$01\bar{1}$	110	$\bar{1}01$	$0\bar{1}\bar{1}$	$1\bar{1}0$	$\bar{1}0\bar{1}$	011	110	101	011	$\bar{1}10$	$10\bar{1}$	$0\bar{1}1$

i, Eq. (21):

$$\boldsymbol{\alpha} = \sum_{i=1}^{18} \varrho_{GND}^{i}\, \mathbf{b}^i \otimes \hat{\mathbf{t}}^i. \tag{21}$$

The line of dislocations; that pierce through an arbitrary area normal, $\mathbf{r}$, and surface S over which the Burgers circuit is constructed, will contribute with their projected value of Burgers vector giving the net Burgers vector, $\mathbf{b}^{net}$. This property of the dislocation tensor can be concluded from the projection in Eq. (22):

$$\mathbf{b}^{net} = \int_S \boldsymbol{\alpha} \cdot \mathbf{r}\, \mathrm{d}S = \int_S \sum_{i=1}^{18} \varrho_{GND}^{i}\, \mathbf{b}^i \otimes \hat{\mathbf{t}}^i \cdot \mathbf{r}\, \mathrm{d}S. \tag{22}$$

The same orientation gradients as in Eq. (21) is computed in terms of the incompatibility of the elastic deformation using Eq. (23) after the application of Stokes theorem to convert the line integral for Burgers circuit to an area integral. Ignoring elastic strains, ϵ_e, the lattice incompatibility is calculated using the rotation gradients only:

$$\mathbf{b}^{net} = \int_S \nabla \times (\mathbf{g} + \epsilon_e) \cdot \mathbf{r}\, \mathrm{d}S \approx \int_S (\nabla \times \mathbf{g}) \cdot \mathbf{r}\, \mathrm{d}S. \tag{23}$$

Setting two Eqs. (22) and (23) equal to each other and cancelling out the integrals, gives the linear relation in Eq. (24):

$$\boldsymbol{\alpha} = \sum_{i=1}^{18} \varrho_{GND}^{i}\, \mathbf{b}^i \otimes \hat{\mathbf{t}}^i = \nabla \times \mathbf{g}. \tag{24}$$

To compute the curl, first the orientation gradients, $[\boldsymbol{\alpha}]$, are recalculated at the element centres using the field variables to give the vector $\{\boldsymbol{\alpha}\}$. Second, the dislocation tensor, $\boldsymbol{\alpha}$, is computed using the orientation gradients. Finally, the GND densities are obtained by two different methods: Least Squares (L2) [51] and Energy Minimization (L1) methods [52] (see Table 1).

2.4.1. GND density calculation by energy minimization (L1) method [52]

In the energy minimization method (L1 method), a solution for Eq. (24) is obtained by direct minimization of total length of dislocations [51]. The dislocation tensor has nine known quantities, allowing a unique solution for nine unknown GND configurations. Therefore, the solution for nine GND densities are searched for among all of the possible unique dislocation configurations, very similar to the work minimization theory by Taylor [53]. The redundant solutions are eliminated by considering the coefficient matrix ($\sum_{i=1}^{9} \mathbf{b}^i \otimes \hat{\mathbf{t}}^i$) of all configurations with a non-zero determinant. As a result, Eq. (24) is slightly modified to give Eq. (25):

$$\sum_{i=1}^{9} \mathbf{b}^i \otimes \hat{\mathbf{t}}^i\, \varrho_{GND}^{i} = \boldsymbol{\alpha}. \tag{25}$$

Once the dislocation densities, ϱ_{GND}^{i},are computed, the overall length of the dislocation is obtained by summing the dislocation segments. The solution with the minimum length is assumed to be the dislocation configuration with minimum energy, Eq. (26):

$$\min(\| \sum_{i=1}^{9} \mathbf{b}^i\, \varrho_{GND}^{i} \|). \tag{26}$$

2.4.2. GND density calculated by the least-squares (L2) method [51]

Eq. (27) is used to compute the GND density, $\{\boldsymbol{\varrho}_{GND}\}$, from the orientation gradients. The $[\mathbf{B}]$ matrix for the solution of Eq. (17) is obtained via the least-squares method (L2):

$$\{\boldsymbol{\varrho}_{GND}\} = [\mathbf{B}]\, \{\boldsymbol{\alpha}\}. \tag{27}$$

Solving with the L2 method provides a B-matrix [51]; its components that are given by Eq. (C.1) in Appendix C.

2.5. Summary of the numerical method

The proposed method, Orientation GRadiEnts using Finite Element Method (OGRE-FEM), is implemented via an in-house code using MATLAB®. The application of the analysis involves several steps that are explained below. The analysis is described for an EBSD dataset, for orientation measurements collected on a square grid.

Step-1 Clean-up the data: Before starting the FE analysis, every data point shall have a proper crystal orientation[2] assigned to perform the integration of $\{\mathbf{q}\}$ in Eq. (18) in every element. Therefore a clean-up algorithm is employed for points without a crystal orientation. The nearest neighbours of those points without crystal orientation are searched and the nearest value is assigned. This procedure is schematically illustrated in Fig. 1. More advanced data clean-up procedures are readily available in other commercial software (AZtecHKL, TSL) or freeware (MTEX [54]), but is considered unnecessary for the analysis method proposed here. Without the data cleanup operation, missing crystal orientation data will yield incorrect results. Therefore, it is an essential to ensure a complete grid of orientations is assigned, with an acceptable error, before proceeding with the analysis.

Step-2 Map all of the axis vectors from the angle-axis pair into the unit stereographic triangle using symmetry, to satisfy the Inequality (3). There are 24 symmetry operators, $\mathbf{O}_k$, for cubic materials which are used in conjunction with Eq. (28) to map the corresponding orientations, $\mathbf{g}'$:

$$\mathbf{g}' = \mathbf{O}_k\, \mathbf{g}\, \mathbf{O}_l^T \quad (k = 1, \ldots, 24; \quad l = 1, \ldots, 24.). \tag{28}$$

Step-3 Create additional degrees of freedom of the field variable for the nodes at the grain boundaries. This is done for each grain boundary to deal with sharp orientation changes. Fig. 2 shows a schematic illustration with the addition of extra nodes at the grain boundaries. Grains are defined by grain identifier numbers (grainID) in the map readily after the cleanup.

Step-4 Apply FE analysis to solve for the orientation field for all of the degrees of freedom, $\{\mathbf{d}\}$, using Eq. (15).

Step-5 Recalculate the orientation gradients at the element centres using interpolation functions through Eq. (19).

Step-6 Calculate GND densities from the orientation gradients at the centre of each element using both (1) L1 and (2) L2 methods.

Step-7 Output the results.

The norm of the GNDs are computed in the post-processing from all the slip systems using Eq. (29):

$$|\varrho| = \| \sum_{i} \mathbf{b}^i\, \varrho_{GND}^{i} \|. \tag{29}$$

[2] Conventional orientation matrix is a passive rotational mapping, that transforms vectors in sample (also referred as laboratory or spatial frame) reference to the crystal (material) reference frame.

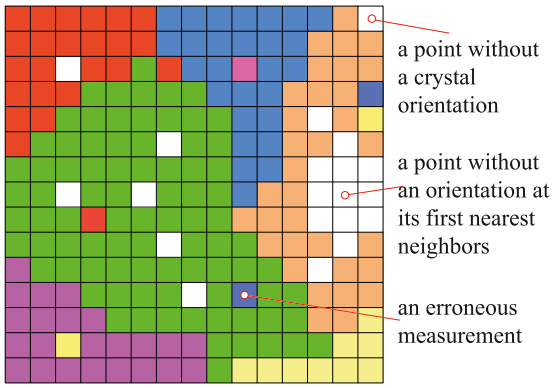

Fig. 1. Schematic illustration of EBSD measurements with experimental artefacts.

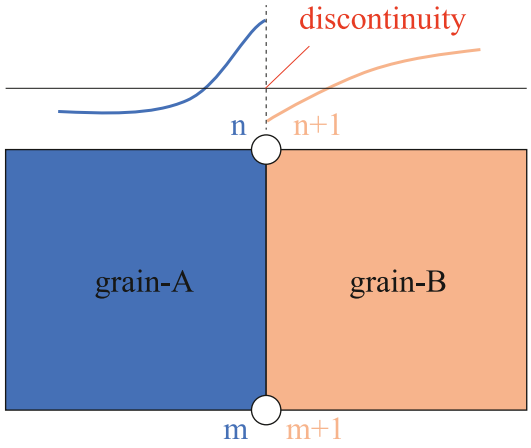

Fig. 2. Schematic of a grain boundary between two differently orientated neighbouring crystals, with additional degrees of freedom assigned to the nodes at the location of the boundary itself.

The MATLAB® scripts are available to public in GitHub® (https://github.com/EralpDemir/OGRE-FEM) together with an example.

3. Experimental

A grade AISI 316L (SS316L) stainless steel sample was polished to a finish with 0.04 μm colloidal silica. The sample was analysed using a Zeiss Merlin field emission gun scanning electron microscope (FEG-SEM) equipped with a Bruker $eFlash^{HR}$ EBSD detector, using Esprit 2.0 software. The microscope was operated with a 10 nA probe current and 20 kV accelerating voltage and high resolution EBSD (HR-EBSD) scans of approximate area of 440 × 240 μm^2 with a step size of 0.5 μm were employed. Diffraction patterns were saved at 800 × 600 $pixel^2$ resolution in 16 bits.

EBSD maps of the SS316L material were obtained in an undeformed state, and an unloaded state after deformation to 0.37% plastic strain. The same region was acquired for each of these maps, using an identical microscope setup and data collection strategy. Fig. 3 shows an example inverse pole figure (IPF-X) map of the undeformed sample. Tensile testing was conducted using a Deben Microtest 5 kN load frame on a dogbone shape specimen with a gauge volume of 1 mm (width) × 1 mm (length) × 1 mm (thickness). The sample was deformed up to a strain of 3.7 × 10-3 at a strain rate of 6 × 10-5 s-1. This corresponded to a maximum stress of 245 MPa, which was just beyond the yield stress of the material. Optical images of the sample surface were acquired during the test using a Hamamatsu ORCA-Spark camera equipped with a Questar QM-100 lens at an acquisition rate of 1 Hz. Using the digital image correlation (DIC) software Ncorr, the macroscopic strain was calculated in the tensile direction [55].

To compare our analysis, GND density maps were computed using cross correlation method described in [56]. This analysis uses a finite difference-based formulation of the L2 method described in Section 2.4.2. The Geometrically Necessary dislocation density is calculated based on the Ref. [51] and its application as performed with HR-EBSD which is outlined in the Ref. [57]. We used this least energy (L2) solution to compare our finite element-based method.

4. Results and discussion

Preliminary analysis was first undertaken to identify the penalty factor, λ, on the orientation gradients using the undeformed EBSD map. For this, a random small region was selected. Fig. 3 shows an IPF-X map for the undeformed SS316L and the selected region within a small window. A mesh is constructed around each EBSD data point as shown in Fig. 4. The grain boundary nodes with multiple degrees of freedom are indicated with red circles in Fig. 4.

A case study is performed to compare the GNDs at the grain boundaries. The example is shown in Fig. 5(a); the presence of steep orientation gradients predict very high GND densities ($>10^{16}\,m^{-2}$) in the vicinity of grain boundaries. Given that this result is obtained from an undeformed specimen, which had been solution annealed, the GND density would be expected to be low ($<10^{12}\ m^{-2}$). It is considered that the high GND density is therefore an artefact of the method without any consideration for the grain boundaries, and is not real. The proposed finite element method accounts for this problem by the inclusion of additional degrees of freedom for the nodes at the grain boundaries. A similar implementation of this was previously demonstrated by Carson and Dawson [46]. The number of degrees of freedom per node, which is the angle-axis pair, was a multiple of the number of grains that connect to that node. This approach allowed for a grain boundary to take multiple values of crystal orientations only at the grain boundaries, thereby avoiding large artificial gradients in those regions. As shown in Fig. 5(b), high GND regions are now eliminated close to grain boundaries when grain boundary nodes are included.

Fig. 6 shows the effect of the penalty parameter, λ, on the continuity of the orientations. As the penalty factor increases, the orientation distribution becomes continuous. The orientation gradients decrease as the penalty on the gradients is raised. This is expected which supports the approach since penalizing the orientation gradients reveals a more continuous orientation field with a lower GND density. In case an excessively high value penalty factor is used, the orientation gradients are lost, resulting in a GND distribution with magnitudes that fall below the measurement floor or noise level. Therefore, the value of the penalty parameter is selected as 10 for the remaining analyses.

The proposed approach is employed to the EBSD dataset from the deformed SS316L sample. A subset region of the map, shown in Fig. 7(a) and Fig. 7(b). The proposed method constructs elements around data points and identifies the grain boundary nodes, Fig. 7(c).

GND distributions using both L1 and L2 methods are computed for the EBSD map of the undeformed SS316L sample, as shown in Fig. 8(a)–(b). The L1 method reveals GND distributions, on average, which are an order magnitude less than the L2 method. The distribution of GNDs of both approach are quite similar though. Because both methods is the linear solution of Eq. (21) which is dependent on the magnitude of $\boldsymbol{\alpha}$. The L1 and L2 giving similar distributions, but there is not a straight linear correlation between the L1 and L2 solutions. The average ratio of norm of the GNDs for L2 to L1 method over the whole map is 13.075 ± 11.603, which has a large variation. Therefore, we cannot conclude a linear correlation between L1 and L2 methods. To further understand the validity of the L1 method, it will be appropriate, in the future, to independently quantify the deformation using alternative methods, such as transmission electron microscopy, where dislocations can be directly measured.

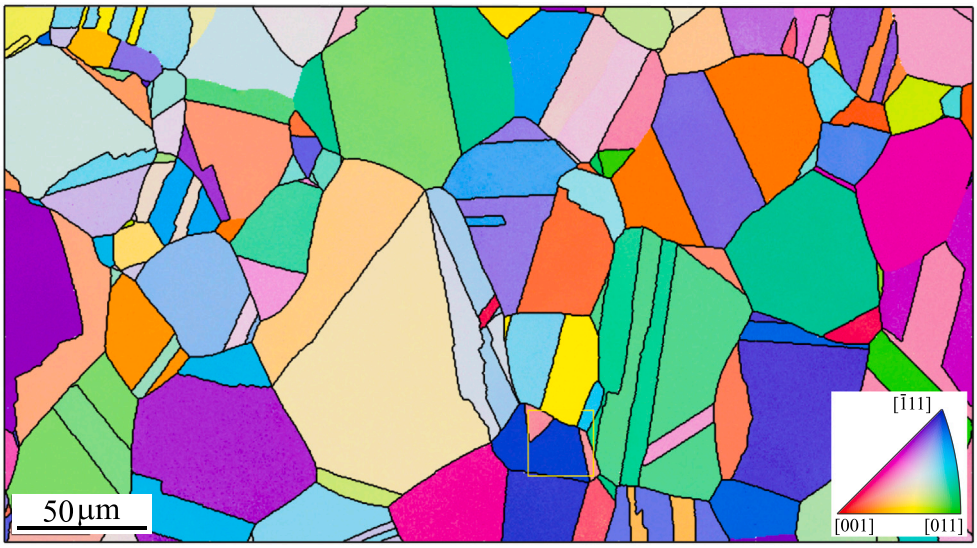

Fig. 3. IPF-X map from EBSD data of undeformed SS316L material. The cropped region indicated with the small window is used for the penalty factor identification.

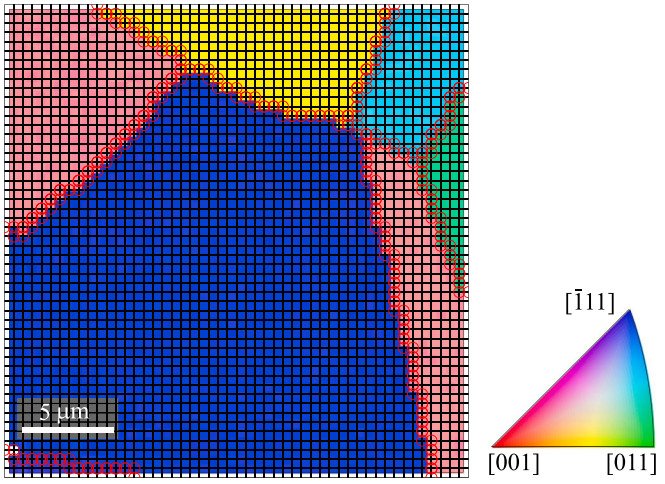

Fig. 4. Mesh constructed for a sub-region from an example EBSD dataset (underformed SS316L). Grain boundary nodes are denoted with red circles. (For interpretation of the references to colour in this figure legend, the reader is referred to the web version of this article.)

For the sample following deformation, Fig. 9 shows the GND density calculations using OGRE-FEM together with a finite difference approach obtained using the L2 method as described in [58]. The proposed method does not possess high GND densities at the grain boundaries, Fig. 9(a). To the contrary, the finite difference approach method does predict high GND densities at the grain and twin boundaries, as shown in Fig. 9(b). Replicating this observation from the undeformed case, these features are believed to be false. The L1 method predicts GND densities over a comparatively narrower range of magnitudes thereby making deformation structures and their distribution at the grain interiors visible. Assuming a GND density of $\sim 10^{12}$ m^{-2} [57] is close to the noise floor of the measurement (with a 200 nm step size), any values below this can be considered as noise. In order to better visualize the grain interiors for the finite difference approach, the dislocation densities above 1.4×10^{13} m^{-2} are set to zero as shown in Fig. 9(c). The same scale as the OGRE-FEM results for better comparison. On average the densities have higher magnitudes in the finite difference result. This shows the effective reduction of noise with the application of OGRE-FEM.

The GND density distributions within the two deformed grains, that are indicated as grain-A and grain-B, is significantly different when the finite element method is used, Fig. 10(a)–(b), compared to the finite element difference method, Fig. 10(c)–(d) and Fig. 10(e)–(f). The maximum GND density is approximately an order of magnitude smaller than that of the finite difference method. The boundary regions of the finite element method are free of the localized, artificially high GND density regions that are present in the finite difference solution. Apart from that, the GND density distributions inside the grains are clearly visible in the finite element method for both grains in Fig. 10(a)–(b). Considering the low tensile strain accumulated in this sample (3.7×10^{-3}), a low GND density (10^{13} m^{-2}) is observed, as may be expected. Detail within this GND density range is not obtained by the finite difference method, and thus the apparent GND structures within the grains are quite different. Therefore, the proposed finite element method helps to visualize the fine dislocation structures with low densities, particularly at low strains. For example, the maxima in grain-B, away from grain boundary, are located at different positions when the two methods are used, Fig. 10(b) and (d). Not withstanding, the proposed approach allows one to visualization the gradients clearly. Note that in Fig. 10(e)–(f) the high GND densities are eliminated by selecting 1.4×10^{13} m^{-2} as the upper limiting value for the dislocation densities. This value is found by the overall that ensures removal of artificial densities at the grain boundaries. The results are plotted using the same scale as the OGRE-FEM findings for easy comparison. The use of upper threshold for the finite difference approach, reduced the maximum densities that are in the grain boundaries, however still the mean density values for the finite difference approach is greater than that the OGRE-FEM reveals.

The grain-average GND density values are processed from the overall GND map and plotted for the misorientation angle (which is computed with respect to the sample reference frame.) in Fig. 11(a) and for the normalized area of the grains (which is the ratio of the area of a grain divided by the area of the largest grain in the map) in Fig. 11(b). The application of finite element and finite difference methods reveal an order of magnitude difference in the average values of GNDs although the general trend is the same for both cases leading to the following common conclusions: The GND density does not correlate with the misorientation angle, Fig. 11(a). Similarly, the distribution scatter homogeneously distributed among the small grains in the finite element

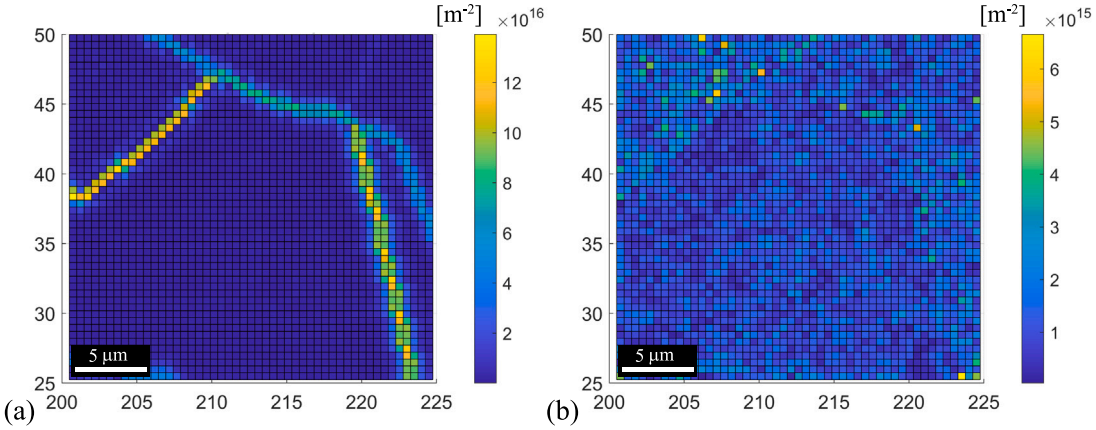

Fig. 5. Norm of GND density distributions; (a) without grain-boundary nodes, (b) with grain-boundary nodes.

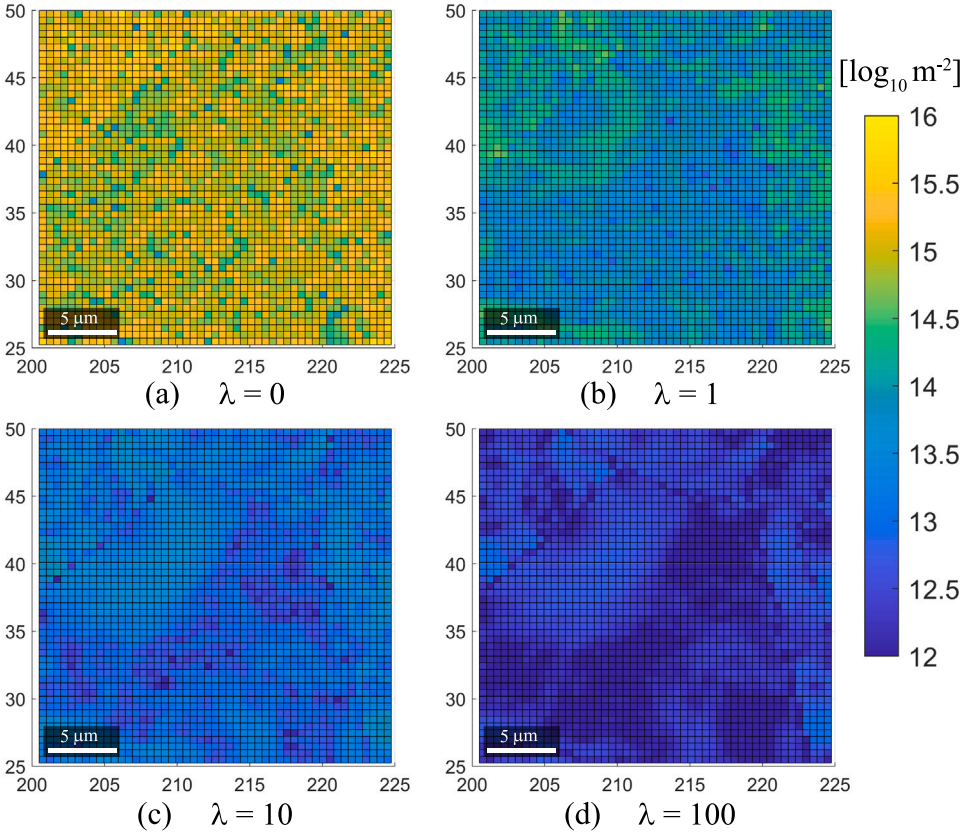

Fig. 6. Norm of GND distributions for penalty parameters of (a) $\lambda = 0$, (b)$\lambda = 1$, (c) $\lambda = 10$, (d) $\lambda = 100$. Colour scale is the decadic logarithm of the GND density. (For interpretation of the references to colour in this figure legend, the reader is referred to the web version of this article.)

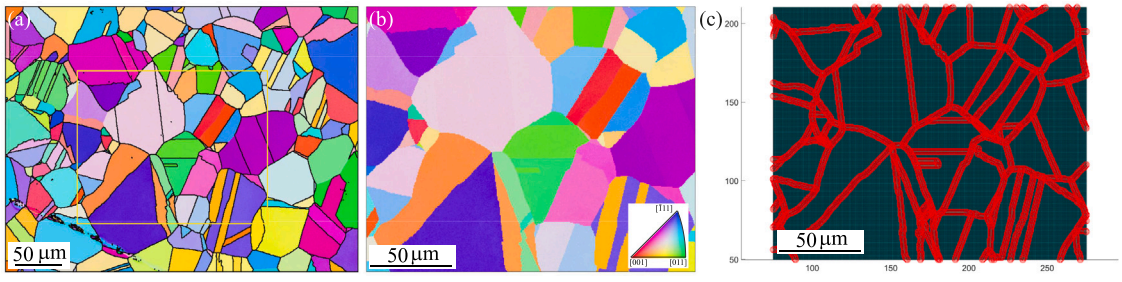

Fig. 7. SS316L before loading; (a) Full EBSD map, (b) Cropped region for analysis, and (c) Mesh with grain-boundary nodes.

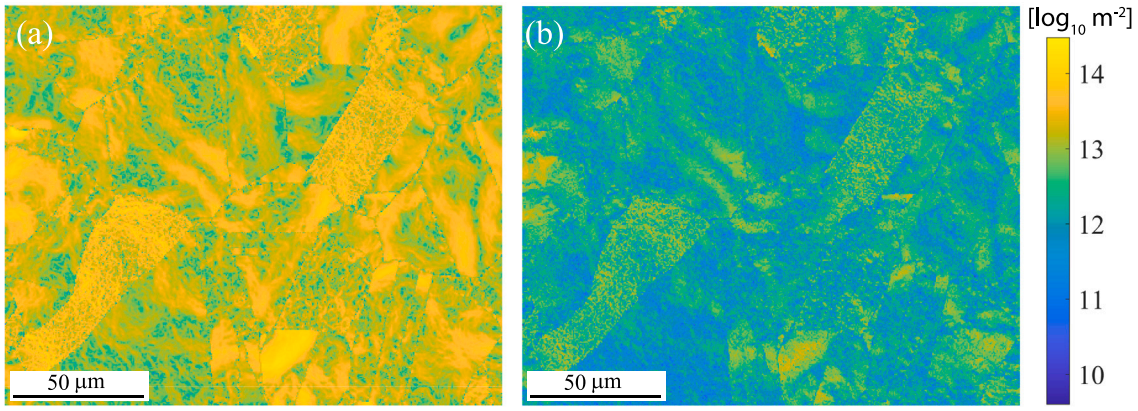

Fig. 8. Norm of GNDs in SS316L before loading obtained by (a) L2 and (b) L1 methods using the proposed finite element framework (OGRE-FEM). Colour bar is in decadic logarithm scale. (For interpretation of the references to colour in this figure legend, the reader is referred to the web version of this article.)

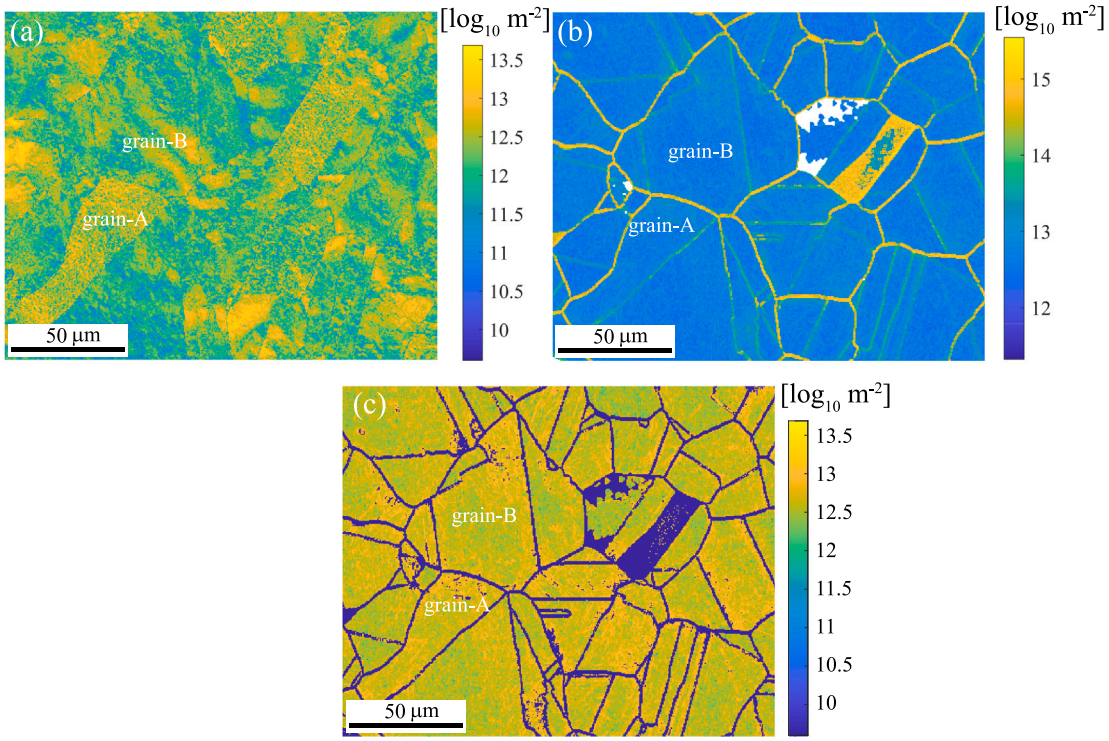

Fig. 9. Norm of GNDs in SS316L after deformation; (a) OGRE-FEM that uses L1 method, (b) a finite difference approach that uses the L2 method, and (c) finite difference results below 1.4×10^{13} m^{-2} density threshold. Colour bar is in decadic logarithm scale. (For interpretation of the references to colour in this figure legend, the reader is referred to the web version of this article.)

method (blue dots) than that of the finite difference approach (red dots), Fig. 11(b). Neither of the method does not show a correlation between GNDs and grain size.

The FE method, showcased here on surface measurements of GND density using EBSD, could be directly applied to measurements of crystal orientation obtained by other diffraction-based methods. Examples include diffraction contrast tomography at lab scale [59], at a synchrotron beamline [60] or dark-field X-ray microscopy [61]. Such future studies would be particularly exciting as they will offer an opportunity to extent the current method to 3D predictions of GND densities.

5. Conclusions

A new method for calculating the GND density for experimental measurements of spatially resolved crystal orientations, here applied to EBSD measurements, has been devised. Testing the methodology on an exemplar polycrystalline sample of SS316L steel, both before and after plastic deformation, the following conclusions can be drawn:

- A finite element (FE) framework was used to calculate the GND density, with additional degrees of freedom assigned to nodes that lie along grain boundaries. This provides accurate intragranular orientation fields which accounts for orientation discontinuities in locations that approach the boundaries. Quantification of GNDs and stresses near the grain boundaries have particular importance in understanding failure mechanisms because the stress build-up and consequent shear banding and/or potential failure occurs near grain boundaries.
- Using an energy minimization (L1) method to calculate the GND densities [52], the maximum per-grain density is predicted to

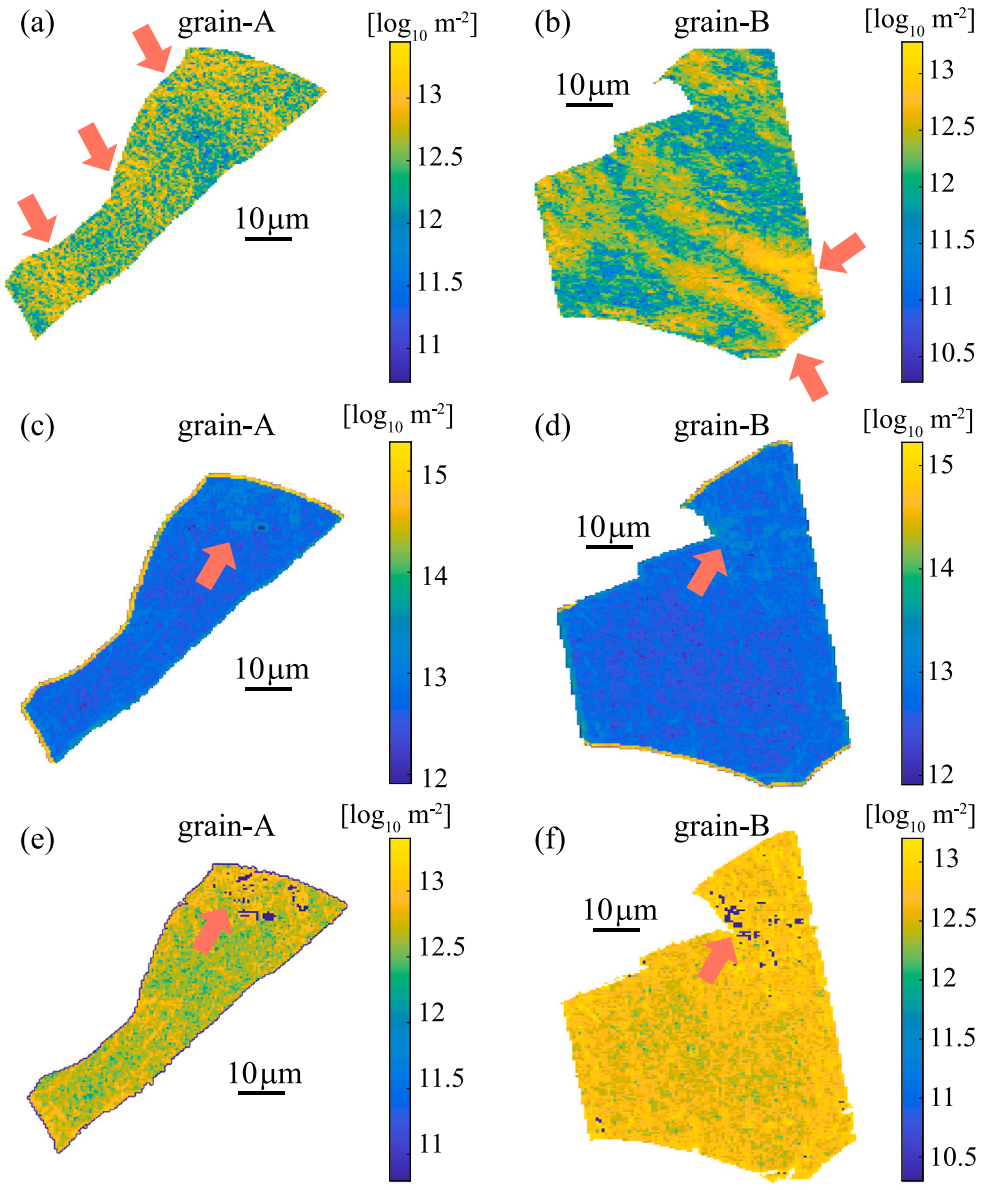

Fig. 10. L2-norm of GNDs in SS316L in two grains after deformation by OGRE-FEM for (a) grain-A, (b) grain-B; by a finite difference approach for (c) grain-A, (d) grain-B, and finite difference results below 1.4×10^{13} m^{-2} density threshold for (e) grain-A, (f) grain-B. The colour bar is in decadic logarithm scale. (For interpretation of the references to colour in this figure legend, the reader is referred to the web version of this article.)

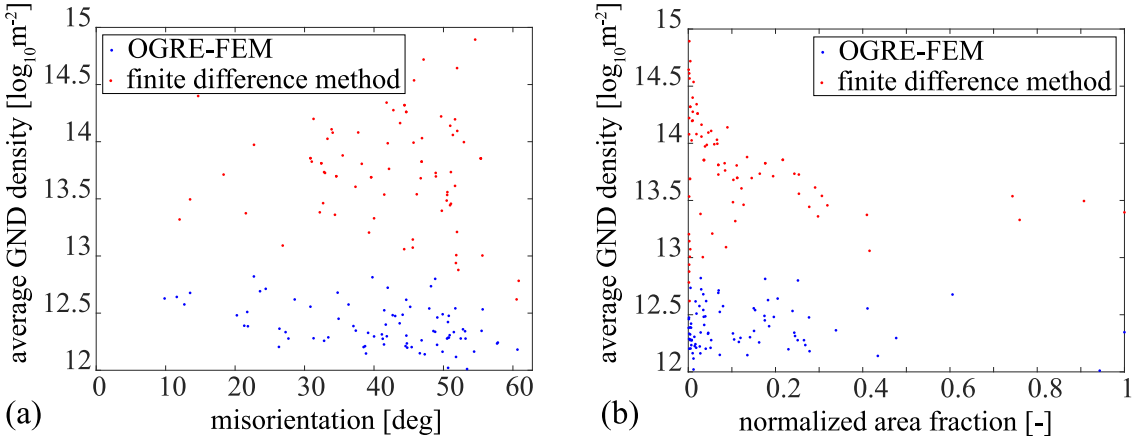

Fig. 11. Analysis of GND density results of the deformed map: average GND density inside grains vs. (a) misorientation of grains with respect to the sample axes (Cube orientation) and (b) normalized area fraction of grains.

be an order of magnitude lower than the commonly used least-squares (L2) method [51] and a linear correlation between the solution of the two methods does not exist.
- The proposed finite element (FE) method is superior to finite difference method since the errors are minimized globally in a consistent framework.
- Very high GND densities are predicted at grain boundaries using the finite difference approach; the artefact arising from the methodology is eliminated when the proposed FE-based method is used. The resulting GND density maps enable the deformation structures to be more easily observed, which will serve as an invaluable tool to characterize features of the plasticity accumulation near grain boundaries or interfaces that controls the macroscopic behaviour of structural materials.

OGRE-FEM is applicable to any polycrystalline material (single or multi phase) or single crystal applications, independent of the measurement technique. The method can be applied to any datasets of spatially resolved orientations, here demonstrated with a surface-based EBSD study, but could be extended to 3D EBSD or XRD measurements in the future.

Declaration of competing interest

The authors declare that they have no known competing financial interests or personal relationships that could have appeared to influence the work reported in this paper.

Acknowledgements

Authors acknowledge funding support from Engineering and Physical Sciences Research Council (EPSRC) of UK with contract no. EP/V038079/1 and EP/R020108/1. We greatly acknowledge insightful discussions with Prof. P.R. Dawson from Cornell University.

Appendix A. Shape functions

Linear quadrilateral elements with isoparametric coordinates of ξ and η are used with the shape functions shown in Eq. (A.1):

$$\begin{aligned} N_1 &= \frac{1}{4}(1-\xi)(1-\eta), \\ N_2 &= \frac{1}{4}(1+\xi)(1-\eta), \\ N_3 &= \frac{1}{4}(1+\xi)(1+\eta), \\ N_4 &= \frac{1}{4}(1-\xi)(1+\eta). \end{aligned} \tag{A.1}$$

Appendix B. Proof of least squares FEM

Suppose there is a field variable $\phi(\mathbf{x})$ defined over a domain. The discrete form of field variable is governed by Eq. (B.1) in which $\{\boldsymbol{\psi}\}$ and $\left\{\widetilde{\boldsymbol{\phi}}\right\}$ represent the weight function and nodal values of the field variable, respectively:

$$\phi(\mathbf{x}) = \{\boldsymbol{\psi}(\mathbf{x})\}\left\{\widetilde{\boldsymbol{\phi}}\right\}. \tag{B.1}$$

Suppose we are given the values of the field variable at certain positions as experimental data within the domain as $\phi_{exp.}$. Then the problem of becomes minimization of the residual in Eq. (B.2):

$$\phi(\mathbf{x}) - \phi_{exp.} = 0. \tag{B.2}$$

Multiplying the residual in Eq. (B.2) with the weight function, which is the same as the interpolation function, gives Eq. (B.3). Note that the interpolation function is position dependent but not shown here for simplicity ($\boldsymbol{\psi} = \boldsymbol{\psi}(\mathbf{x})$):

$$\{\boldsymbol{\psi}\}^T \phi(\mathbf{x}) - \{\boldsymbol{\psi}\}^T \phi_{exp.} = 0. \tag{B.3}$$

Integrating over the domain Ω and rearranging the terms, the residual becomes as in Eq. (B.4):

$$\int_\Omega \{\boldsymbol{\psi}\}^T \phi(\mathbf{x})\,\mathrm{d}\Omega = \int_\Omega \{\boldsymbol{\psi}\}^T \phi_{exp.}\,\mathrm{d}\Omega. \tag{B.4}$$

Substituting the expression for discretized field variable in Eq. (B.1), the residual takes the form in Eq. (B.5):

$$\int_\Omega \{\boldsymbol{\psi}\}^T \{\boldsymbol{\psi}\}\left\{\widetilde{\boldsymbol{\phi}}\right\}\mathrm{d}\Omega = \int_\Omega \{\boldsymbol{\psi}\}^T \phi_{exp.}\,\mathrm{d}\Omega. \tag{B.5}$$

Eq. (B.5) is analogous to Eq. (15) without the gradient constraint. Similarly, $[\mathbf{Y}]$ and $\{\mathbf{z}\}$ represent the mass-like matrix and pseudo-force vector revealing the linear problem in Eq. (B.6):

$$[\mathbf{Y}]\left\{\widetilde{\boldsymbol{\phi}}\right\} = \{\mathbf{z}\}. \tag{B.6}$$

Field solution is obtained via Eq. (B.7):

$$\{\boldsymbol{\phi}\} = [\mathbf{Y}]^{-1}\{\mathbf{z}\}. \tag{B.7}$$

The weak form of the gradient of the field is obtained similarly.

Appendix C. B-matrix in the reference [51]

Eq. (C.1) shows the B-matrix used to compute the GNDs.

A misprint in the expression of $[\mathbf{B}]$ in the original Ref. [51] is noted for the element indicated here with an asterisk (see row 11, column 9). The value is necessarily positive, however, a negative premultiplier was used for the same element in the Ref. [45].

$$[\mathbf{B}] = \begin{bmatrix} a & 7c & -13c & -7c & -a & 13c & c & -c & 0 \\ -a & 13c & -7c & -c & 0 & c & 7c & -13c & a \\ 0 & c & -c & -13c & a & 7c & 13c & -7c & -a \\ a & -7c & 13c & 7c & -a & 13c & -c & -c & 0 \\ -a & -13c & 7c & c & 0 & c & -7c & -13c & a \\ 0 & -c & c & 13c & a & 7c & -13c & -7c & -a \\ a & -7c & -13c & 7c & -a & -13c & c & c & 0 \\ -a & -13c & -7c & c & 0 & -c & 7c & 13c & a \\ 0 & -c & -c & 13c & a & -7c & 13c & 7c & -a \\ a & 7c & 13c & -7c & -a & -13c & -c & c & 0 \\ -a & 13c & 7c & -c & 0 & -c & -7c & 13c & a^* \\ 0 & c & c & -13c & a & -7c & -13c & 7c & -a \\ 5d & e & 0 & e & 5d & 0 & 0 & 0 & -d \\ 5d & 0 & e & 0 & -d & 0 & e & 0 & 5d \\ -d & 0 & 0 & 0 & 5d & e & 0 & e & 5d \\ 5d & -e & 0 & -e & 5d & 0 & 0 & 0 & -d \\ 5d & 0 & -e & 0 & -d & 0 & -e & 0 & 5d \\ -d & 0 & 0 & 0 & 5d & -e & 0 & -e & 5d \end{bmatrix} \tag{C.1}$$

where $a = \sqrt{3}/9$, $c = \sqrt{3}/84$, $d = 1/18$, $e = 3/14$ as in the Ref. [51].

References

[1] N. Fleck, G. Muller, M.F. Ashby, J.W. Hutchinson, Strain gradient plasticity: theory and experiment, Acta Metallurgica Et Materialia 42 (2) (1994) 475–487.
[2] H. Gao, Y. Huang, W. Nix, J. Hutchinson, Mechanism-based strain gradient plasticity—I. Theory, J. Mech. Phys. Solids 47 (6) (1999) 1239–1263.
[3] M. Calcagnotto, D. Ponge, E. Demir, D. Raabe, Orientation gradients and geometrically necessary dislocations in ultrafine grained dual-phase steels studied by 2D and 3D EBSD, Mater. Sci. Eng. A 527 (10–11) (2010) 2738–2746.
[4] P. Littlewood, T. Britton, A. Wilkinson, Geometrically necessary dislocation density distributions in Ti–6Al–4V deformed in tension, Acta Mater. 59 (16) (2011) 6489–6500.
[5] K. Cheong, E. Busso, A. Arsenlis, A study of microstructural length scale effects on the behaviour of FCC polycrystals using strain gradient concepts, Int. J. Plast. 21 (9) (2005) 1797–1814.
[6] G. Gottstein, Physical Foundations of Materials Science, Springer Science & Business Media, 2013.
[7] J.F. Nye, Some geometrical relations in dislocated crystals, Acta Metall. 1 (2) (1953) 153–162.

[8] H. Gao, Y. Huang, Geometrically necessary dislocation and size-dependent plasticity, Scr. Mater. 48 (2) (2003) 113–118.

[9] C. Bayley, W. Brekelmans, M. Geers, A comparison of dislocation induced back stress formulations in strain gradient crystal plasticity, Int. J. Solids Struct. 43 (24) (2006) 7268–7286.

[10] A. Ma, F. Roters, D. Raabe, A dislocation density based constitutive model for crystal plasticity FEM including geometrically necessary dislocations, Acta Mater. 54 (8) (2006) 2169–2179.

[11] F. Dunne, A. Walker, D. Rugg, A systematic study of hcp crystal orientation and morphology effects in polycrystal deformation and fatigue, Proc. R. Soc. A Math. Phys. Eng. Sci. 463 (2082) (2007) 1467–1489.

[12] J. Segurado, R.A. Lebensohn, J. LLorca, Computational homogenization of polycrystals, Adv. Appl. Mech. 51 (2018) 1–114.

[13] S. Das, F. Hofmann, E. Tarleton, Consistent determination of geometrically necessary dislocation density from simulations and experiments, Int. J. Plast. 109 (2018) 18–42.

[14] H. Dai, Geometrically-Necessary Dislocation Density in Continuum Plasticity Theory, FEM Implementation and Applications (Ph.D. thesis), Massachusetts Institute of Technology, 1997.

[15] L. Evers, W. Brekelmans, M. Geers, Non-local crystal plasticity model with intrinsic SSD and GND effects, J. Mech. Phys. Solids 52 (10) (2004) 2379–2401.

[16] J.M. Gerken, P.R. Dawson, A crystal plasticity model that incorporates stresses and strains due to slip gradients, J. Mech. Phys. Solids 56 (4) (2008) 1651–1672.

[17] A. Acharya, J. Bassani, Lattice incompatibility and a gradient theory of crystal plasticity, J. Mech. Phys. Solids 48 (8) (2000) 1565–1595.

[18] A. Arsenlis, D.M. Parks, R. Becker, V.V. Bulatov, On the evolution of crystallographic dislocation density in non-homogeneously deforming crystals, J. Mech. Phys. Solids 52 (6) (2004) 1213–1246.

[19] C. Reuber, P. Eisenlohr, F. Roters, D. Raabe, Dislocation density distribution around an indent in single-crystalline nickel: Comparing nonlocal crystal plasticity finite-element predictions with experiments, Acta Mater. 71 (2014) 333–348.

[20] E. Demir, I. Gutierrez-Urrutia, Investigation of strain hardening near grain boundaries of an aluminum oligocrystal: experiments and crystal based finite element method, Int. J. Plast. 136 (2021) 102898.

[21] P. Cermelli, M.E. Gurtin, On the characterization of geometrically necessary dislocations in finite plasticity, J. Mech. Phys. Solids 49 (7) (2001) 1539–1568.

[22] F. Lagattu, F. Bridier, P. Villechaise, J. Brillaud, In-plane strain measurements on a microscopic scale by coupling digital image correlation and an in situ SEM technique, Mater. Charact. 56 (1) (2006) 10–18.

[23] M. Tschopp, B. Bartha, W. Porter, P. Murray, S. Fairchild, Microstructure-dependent local strain behavior in polycrystals through in-situ scanning electron microscope tensile experiments, Metall. Mater. Trans. A 40 (10) (2009) 2363–2368.

[24] C. Efstathiou, H. Sehitoglu, J. Lambros, Multiscale strain measurements of plastically deforming polycrystalline titanium: Role of deformation heterogeneities, Int. J. Plast. 26 (1) (2010) 93–106.

[25] A.J. Wilkinson, G. Meaden, D.J. Dingley, High-resolution elastic strain measurement from electron backscatter diffraction patterns: new levels of sensitivity, Ultramicroscopy 106 (4–5) (2006) 307–313.

[26] C.J. Gardner, B.L. Adams, J. Basinger, D.T. Fullwood, EBSD-based continuum dislocation microscopy, Int. J. Plast. 26 (8) (2010) 1234–1247.

[27] T. Zhang, D.M. Collins, F.P. Dunne, B.A. Shollock, Crystal plasticity and high-resolution electron backscatter diffraction analysis of full-field polycrystal Ni superalloy strains and rotations under thermal loading, Acta Mater. 80 (2014) 25–38.

[28] B. El-Dasher, B. Adams, A. Rollett, Experimental recovery of geometrically necessary dislocation density in polycrystals, Scr. Mater. 48 (2) (2003) 141–145.

[29] D. Field, P. Trivedi, S. Wright, M. Kumar, Analysis of local orientation gradients in deformed single crystals, Ultramicroscopy 103 (1) (2005) 33–39.

[30] A. Wilkinson, E. Clarke, T. Britton, P. Littlewood, P. Karamched, High-resolution electron backscatter diffraction: an emerging tool for studying local deformation, J. Strain Anal. Eng. Des. 45 (5) (2010) 365–376.

[31] W. Pantleon, Resolving the geometrically necessary dislocation content by conventional electron backscattering diffraction, Scr. Mater. 58 (11) (2008) 994–997.

[32] W. Ludwig, A. King, P. Reischig, M. Herbig, E.M. Lauridsen, S. Schmidt, H. Proudhon, S. Forest, P. Cloetens, S.R. Du Roscoat, et al., New opportunities for 3D materials science of polycrystalline materials at the micrometre lengthscale by combined use of X-ray diffraction and X-ray imaging, Mater. Sci. Eng. A 524 (1–2) (2009) 69–76.

[33] Y. Guo, D.M. Collins, E. Tarleton, F. Hofmann, A.J. Wilkinson, T.B. Britton, Dislocation density distribution at slip band-grain boundary intersections, Acta Mater. 182 (2020) 172–183.

[34] C. Yildirim, C. Jessop, J. Ahlström, C. Detlefs, Y. Zhang, 3D mapping of orientation variation and local residual stress within individual grains of pearlitic steel using synchrotron dark field X-ray microscopy, Scr. Mater. (ISSN: 1359-6462) 197 (2021) 113783, http://dx.doi.org/10.1016/j.scriptamat.2021.113783.

[35] P.S. Karamched, A.J. Wilkinson, High resolution electron back-scatter diffraction analysis of thermally and mechanically induced strains near carbide inclusions in a superalloy, Acta Mater. 59 (1) (2011) 263–272.

[36] J. Jiang, T. Britton, A. Wilkinson, Evolution of dislocation density distributions in copper during tensile deformation, Acta Mater. 61 (19) (2013) 7227–7239.

[37] J. Jiang, T. Britton, A. Wilkinson, Measurement of geometrically necessary dislocation density with high resolution electron backscatter diffraction: effects of detector binning and step size, Ultramicroscopy 125 (2013) 1–9.

[38] S. Birosca, F. Di Gioacchino, S. Stekovic, M. Hardy, A quantitative approach to study the effect of local texture and heterogeneous plastic strain on the deformation micromechanism in RR1000 nickel-based superalloy, Acta Mater. 74 (2014) 110–124.

[39] A. Kundu, D.P. Field, Influence of plastic deformation heterogeneity on development of geometrically necessary dislocation density in dual phase steel, Mater. Sci. Eng. A 667 (2016) 435–443.

[40] C. Moussa, M. Bernacki, R. Besnard, N. Bozzolo, Statistical analysis of dislocations and dislocation boundaries from EBSD data, Ultramicroscopy 179 (2017) 63–72.

[41] O. Muransky, L. Balogh, M. Tran, C. Hamelin, J.-S. Park, M.R. Daymond, On the measurement of dislocations and dislocation substructures using EBSD and HRSD techniques, Acta Mater. 175 (2019) 297–313.

[42] S. Birosca, G. Liu, R. Ding, J. Jiang, T. Simm, C. Deen, M. Whittaker, The dislocation behaviour and GND development in a nickel based superalloy during creep, Int. J. Plast. 118 (2019) 252–268.

[43] S. Kalácska, Z. Dankházi, G. Zilahi, X. Maeder, J. Michler, P.D. Ispánovity, I. Groma, Investigation of geometrically necessary dislocation structures in compressed Cu micropillars by 3-dimensional HR-EBSD, Mater. Sci. Eng. A 770 (2020) 138499.

[44] P.J. Konijnenberg, S. Zaefferer, D. Raabe, Assessment of geometrically necessary dislocation levels derived by 3D EBSD, Acta Mater. 99 (2015) 402–414.

[45] W.A. Witzen, A.T. Polonsky, T.M. Pollock, I.J. Beyerlein, Three-dimensional maps of geometrically necessary dislocation densities in additively manufactured Ni-based superalloy IN718, Int. J. Plast. 131 (2020) 102709.

[46] R. Carson, P. Dawson, Formulation and characterization of a continuous crystal lattice orientation finite element method (LOFEM) and its application to dislocation fields, J. Mech. Phys. Solids 126 (2019) 1–19.

[47] O.C. Zienkiewicz, R.L. Taylor, The Finite Element Method for Solid and Structural Mechanics, Elsevier, 2005.

[48] K.P. McNelis, P.R. Dawson, M.P. Miller, A two-scale methodology for determining the residual stresses in polycrystalline solids using high energy X-ray diffraction data, J. Mech. Phys. Solids 61 (2) (2013) 428–449.

[49] E. Demir, J.-S. Park, M. Miller, P. Dawson, A computational framework for evaluating residual stress distributions from diffraction-based lattice strain data, Comput. Methods Appl. Mech. Engrg. 265 (2013) 120–135.

[50] E. Demir, H.S. Sas, M. Isik, E.A. Gungor, K. Davut, A numerical methodology for monitoring stress distributions and experimental proof of the concept on metal embedded thin polymer-matrix composites using X-ray diffraction, Thin-Walled Struct. 173 (2022) 108942.

[51] A. Arsenlis, D. Parks, Crystallographic aspects of geometrically-necessary and statistically-stored dislocation density, Acta Mater. 47 (5) (1999) 1597–1611.

[52] E. Demir, D. Raabe, N. Zaafarani, S. Zaefferer, Investigation of the indentation size effect through the measurement of the geometrically necessary dislocations beneath small indents of different depths using EBSD tomography, Acta Mater. 57 (2) (2009) 559–569.

[53] G.I. Taylor, Plastic strain in metals, J. Inst. Metals 62 (1938) 307–324.

[54] F. Bachmann, R. Hielscher, H. Schaeben, Texture analysis with MTEX–free and open source software toolbox, in: Solid State Phenomena, 160, Trans Tech Publ, 2010, pp. 63–68.

[55] J. Blaber, B. Adair, A. Antoniou, Ncorr: open-source 2D digital image correlation matlab software, Exp. Mech. 55 (6) (2015) 1105–1122.

[56] A.J. Wilkinson, T.B. Britton, Strains, planes, and EBSD in materials science, Mater. Today 15 (9) (2012) 366–376.

[57] A.J. Wilkinson, D. Randman, Determination of elastic strain fields and geometrically necessary dislocation distributions near nanoindents using electron back scatter diffraction, Phil. Mag. 90 (9) (2010) 1159–1177.

[58] D. Agius, A. Kareer, A.A. Mamun, C. Truman, D.M. Collins, M. Mostafavi, D. Knowles, A crystal plasticity model that accounts for grain size effects and slip system interactions on the deformation of austenitic stainless steels, Int. J. Plast. 152 (2022) 103249.

[59] S.A. McDonald, T.L. Burnett, J. Donoghue, N. Gueninchault, H. Bale, C. Holzner, E.M. Lauridsen, P.J. Withers, Tracking polycrystal evolution non-destructively in 3D by laboratory X-ray diffraction contrast tomography, Mater. Charact. 172 (2021) 110814.

[60] L. Nervo, A. King, A. Fitzner, W. Ludwig, M. Preuss, A study of deformation twinning in a titanium alloy by X-ray diffraction contrast tomography, Acta Mater. 105 (2016) 417–428.

[61] C. Yildirim, D. Brellier, R. Pesci, F. Boulard, N. Baier, T. Zhou, T. Nguyen-Thanh, P. Gergaud, T. Schulli, P. Ballet, In-situ mapping of local orientation and strain in a fully operable infrared sensor, Acta Mater. 220 (2021) 117290.